The Astrophysical Journal Supplement Series, 262:50 (11pp), 2022 October https://doi.org/10.3847/1538-4365/ac8d66

Improved AI-generated Solar Farside Magnetograms by STEREO and SDO Data Sets and Their Release

Hyun-Jin Jeong[1], Yong-Jae Moon[1,2], Eunsu Park[3], Harim Lee[2], and Ji-Hye Baek[3,4]
[1] School of Space Research, Kyung Hee University, Yongin, 17104, Republic of Korea; moonyj@khu.ac.kr
[2] Department of Astronomy and Space Science, College of Applied Science, Kyung Hee University, Yongin, 17104, Republic of Korea
[3] Space Science Division, Korea Astronomy and Space Science Institute, Daejeon, 34055, Republic of Korea
[4] Technology Center for Astronomy and Space Science, Korea Astronomy and Space Science Institute, Daejeon, 34055, Republic of Korea
Received 2022 April 24; revised 2022 August 24; accepted 2022 August 26; published 2022 October 7

Abstract

Here we greatly improve artificial intelligence (AI)–generated solar farside magnetograms using data sets from the Solar Terrestrial Relations Observatory (STEREO) and Solar Dynamics Observatory (SDO). We modify our previous deep-learning model and configuration of input data sets to generate more realistic magnetograms than before. First, our model, which is called Pix2PixCC, uses updated objective functions, which include correlation coefficients (CCs) between the real and generated data. Second, we construct input data sets of our model: solar farside STEREO extreme-ultraviolet (EUV) observations together with nearest frontside SDO data pairs of EUV observations and magnetograms. We expect that the frontside data pairs provide historic information on magnetic field polarity distributions. We demonstrate that magnetic field distributions generated by our model are more consistent with the real ones than previously, in consideration of several metrics. The averaged pixel-to-pixel CC for full disk, active regions, and quiet regions between real and AI-generated magnetograms with 8×8 binning are 0.88, 0.91, and 0.70, respectively. Total unsigned magnetic flux and net magnetic flux of the AI-generated magnetograms are consistent with those of real ones for the test data sets. It is interesting to note that our farside magnetograms produce polar field strengths and magnetic field polarities consistent with those of nearby frontside magnetograms for solar cycles 24 and 25. Now we can monitor the temporal evolution of active regions using solar farside magnetograms by the model together with the frontside ones. Our AI-generated solar farside magnetograms are now publicly available at the Korean Data Center for SDO (http://sdo.kasi.re.kr).

Unified Astronomy Thesaurus concepts: Solar magnetic fields (1503); Convolutional neural networks (1938); The Sun (1693); Astronomy data analysis (1858)

Supporting material: animations

1. Introduction

Magnetic fields play a fundamental role in producing solar extreme events, i.e., solar flares and coronal mass ejections (Wiegelmann et al. 2014; Judge et al. 2021). A series of ground-based and space-borne magnetographs have provided solar magnetic field data to study the field's origin and evolution over the last few decades (Pietarila et al. 2013). The solar magnetograph is an instrument producing a map of magnetic field strength and/or direction on the Sun, which is called a magnetogram (Babcock 1953). The Helioseismic and Magnetic Imager (HMI; Scherrer et al. 2012) on board SDO, which is in geosynchronous orbit, has provided high-resolution magnetograms of the entire solar disk. Recently, the Polarimetric and Helioseismic Imager (Solanki et al. 2020) on board Solar Orbiter started obtaining data of photospheric fields from outside the Sun–Earth line (Müller et al. 2020).

Before the Solar Orbiter mission, twin STEREO spacecraft provided the first stereoscopic view of the Sun drifting ahead of and behind the Earth's orbit (Kaiser et al. 2008). The STEREO Ahead (A) and Behind (B) were launched in 2006 and offered a complete 360° view of the entire Sun with frontside observations. The STEREO data, together with the SDO data, have been widely used to study solar atmospheric phenomena in three dimensions (Sterling et al. 2012; Caplan et al. 2016; Zhou et al. 2021). However, because they did not include a magnetograph, studies of magnetic activities from the frontside to the farside of the Sun were limited during the STEREO era.

Kim et al. (2019; hereafter KPL19) generated solar farside magnetograms from the STEREO/Extreme UltraViolet Imager (EUVI; Howard et al. 2008) 304 Å observations using deep learning. KPL19 applied the Pix2Pix model (Isola et al. 2017), which is a widely used deep-learning model in image translation tasks. They trained and evaluated the model with pairs of solar frontside SDO/Atmospheric Imaging Assembly (AIA; Lemen et al. 2011) 304 Å observations and SDO/HMI line-of-sight (LOS) 720 s magnetograms. Results of KPL19 showed that the farside magnetograms could be used to monitor the temporal evolution of active regions (ARs). However they set the upper and lower saturation limits of the field strength at ±100 G, because their model worked well with proper byte scaling (Park et al. 2021). Their model generated the distributions and shapes of the ARs well, but it was hard to produce original-scale magnetic fluxes (Liu et al. 2021). Jeong et al. (2020; hereafter J20) improved the AI-generated magnetograms using an upgraded deep-learning approach with ±3000 G dynamic range based on the Pix2PixHD model (Wang et al. 2018) and multichannel SDO/AIA images of 171, 195, and 304 Å for the model input. J20 showed that their results could reproduce strong magnetic fluxes and the

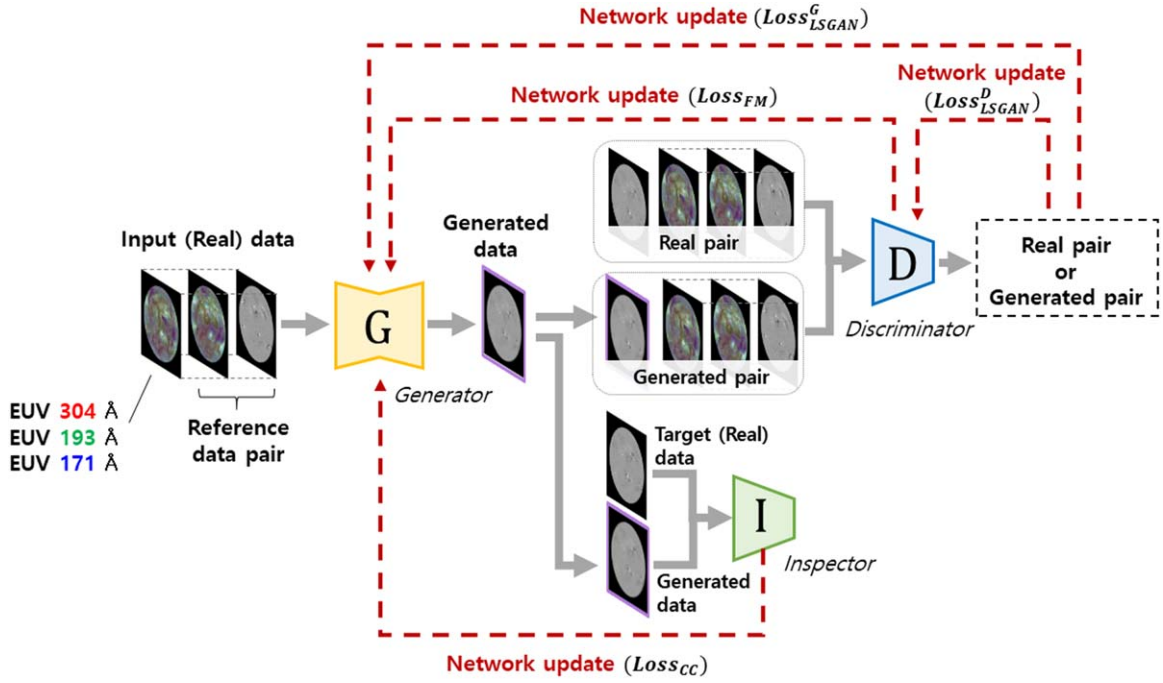

Figure 1. Flowchart and structures of the Pix2PixCC model. *G*, *D*, and *I* are the generator, discriminator, and inspector, respectively. The generator produces target-like data from input data. When we train the model, input data are SDO/AIA EUV 304, 193, and 171 Å images and a reference data pair. The reference data pair is composed of the three SDO EUV images and the corresponding SDO/HMI magnetogram, which are the nearest available ones. The discriminator trains for distinguishing between the real pair and generated pair. The real pair consists of an input data and a target data, and the generated pair consists of an input data and a generated data. The inspector computes CCs between the target data and generated data. The generator and discriminator are updated from the losses calculated from the inspector and discriminator.

distribution of polarities for not only ARs, but also quiet regions (QRs). They applied the AI-generated farside ones to a part of the boundary conditions for the extrapolation of coronal magnetic fields. Results of the application were much more consistent with coronal farside extreme-UV (EUV) observations than those of the conventional method.

In the present study, we generate more accurate solar farside magnetograms than those of KPL19 and J20. For this, we make an upgraded model including a correlation coefficient (CC)–based objective with additional input data: not only farside STEREO EUV images but also frontside data pairs of SDO/AIA EUV images and HMI magnetograms as reference information. In this paper, we call the farside data generated by KPL19 AISFM 1.0, the data generated by J20 AISFM 2.0, and our data AISFM 3.0, respectively. We describe the detailed structure of our model in Section 2, and describe our data configurations in Section 3. We show our evaluation results of the model trained with the frontside evaluation data sets in Section 4.1. Then we generate AISFMs by the model from the corresponding images of STEREO A (or B) and the frontside reference data pairs, and show the results in Section 4.2. We release the AISFMs 3.0 and describe the data in Section 5. We conclude our study in Section 6.

2. Deep-learning Model

We use a deep-learning model called the Pix2PixCC model to generate solar farside magnetograms from the farside EUV observations and reference data pairs. Figure 1 shows the main structure of our model. The model consists of three major components: a generator (*G*), a discriminator (*D*), and an inspector (*I*). The generator is a generative network, and tries to produce target-like data from inputs with the help of the discriminator and the inspector. The discriminator is a discriminative network, which attempts to distinguish between the more realistic pair between a real pair and a generated pair. The real pair consists of input data and target data. The generated pair consists of input data and output from the generator. The generator gets updated with objectives from the discriminator, and tries to generate the best outputs to fool the discriminator. The inspector computes CCs between the target data and output from the generator to produce realistic values for the generated ones.

The generator and discriminator are multilayer networks. The multiple layers of the generative network are composed of several convolutional and transposed-convolutional filters of which parameters are updated during the model training process. Briefly, the convolutional filters try to extract features automatically from the input data, and the transposed-convolutional filters attempt to reconstruct outputs from the extracted features. For the detailed function of the filters in the network, refer to Goodfellow et al. (2016) and Buduma & Locascio (2017). The discriminative network consists of several convolution layers. Each convolution layer generates a feature map based on input. Our model has a feature matching (FM) loss ($\mathrm{Loss_{FM}}$), which is an objective function to optimize the parameters of the generator. The FM loss is to minimize the absolute difference between the feature maps of the real and generated pair from multiple layers of the discriminator. It is more effective for a large dynamic range of data than the loss function derived from the absolute difference between the target and generated data directly (Rana et al. 2019; Marnerides et al. 2021). The objective function $\mathrm{Loss_{FM}}$ is given by

$$\mathrm{Loss_{FM}}(G, D) = \sum_{i=1}^{T} \frac{1}{N_i} \| D^{(i)}(x, y) - D^{(i)}(x, G(x)) \|, \quad (1)$$

where x, y, T, i, and N_i are input data, target data, the total number of layers, the serial number of the layers, and the number of elements in output feature maps of each layer, respectively. $G(x)$ means output data from the generator. $D^{(i)}$ denotes the ith-layer feature extractor of the discriminator.

Our networks use least-squares generative adversarial network (LSGAN) losses (Mao et al. 2017). The LSGAN losses update the generator ($\text{Loss}^G_{\text{LSGAN}}$) and the discriminator ($\text{Loss}^D_{\text{LSGAN}}$), and are obtained by

$$\begin{aligned}\text{Loss}^G_{\text{LSGAN}}(G, D) &= \frac{1}{2}(D(x, G(x)) - 1)^2 \\ \text{Loss}^D_{\text{LSGAN}}(G, D) &= \frac{1}{2}(D(x, y) - 1)^2 + \frac{1}{2}(D(x, G(x)))^2,\end{aligned} \tag{2}$$

where $D(x, y)$ and $D(x, G(x))$ are probabilities in the range of 0 (generated) to 1 (real) at the end of the discriminator from the real pair and generated pair, respectively. The generator tries to minimize the $\text{Loss}^G_{\text{LSGAN}}$, and the discriminator tries to minimize $\text{Loss}^D_{\text{LSGAN}}$. The competition between the generator and the discriminator contributes to the generation of realistic data. The performance of the adversarial objectives has been well demonstrated in image-to-image translation tasks for solar data (Park et al. 2019; Shin et al. 2020; Lim et al. 2021; Son et al. 2021).

In order for stable training of the generator, we use an additional objective function called CC loss (Loss_{CC}). It is known that the CC-based loss function has performed better than error-based loss functions: mean squared error, mean absolute error, etc. (Vallejos et al. 2020; Atmaja & Akagi 2021). We use Lin's concordance CC, which takes bios into Pearson's CC (Lawrence & Lin 1989). The concordance CC is commonly used to assess the reproducibility evaluating the degree to which pairs of data fall on the 45° line through the origin. The range of concordance CC is from −1 (perfect disagreement) to 1 (perfect agreement). The inspector computes the CC loss with multiscale target and generated data. The function of Loss_{CC}, which maximizes the agreement between the target and generated data, is defined as

$$\text{Loss}_{\text{CC}}(G) = \sum_{i=0}^{T} \frac{1}{T+1}(1 - CC_i(y, G(x))), \tag{3}$$

where T and i are the total number of downsampling by a factor of two and the serial number of the downsampling, respectively. CC_i means the CC value between the 2^i times downsampled target and AI-generated data. The average of the CC values from the multiscale target and generated data helps the model to optimize the network parameters. In addition, with the help of Loss_{CC}, we do not impose artificial saturation limits on our model.

Our final objectives are as follows:

$$\begin{aligned}&\min_G \lambda_1 \text{Loss}^G_{\text{LSGAN}}(G, D) + \lambda_2 \text{Loss}_{\text{FM}}(G, D) \\ &+ \lambda_3 \text{Loss}_{\text{CC}}(G) \\ &\min_D \text{Loss}^D_{\text{LSGAN}}(G, D),\end{aligned} \tag{4}$$

where λ_1, λ_2, and λ_3 are hyperparameters that control the importance of $\text{Loss}^G_{\text{LSGAN}}$, Loss_{FM}, and Loss_{CC}, respectively. We use 2, 10, and 5 for λ_1, λ_2, and λ_3, respectively.

The purpose of the generative adversarial network (GAN) objectives is to generate an answer that is acceptable. It is designed to deal with the probability space of the output. Wang et al. (2018) improved the GAN objectives by incorporating the FM objective to produce stable outputs. They set the importance of the FM loss (λ_2) to be higher than that of the GAN loss (λ_1). In J20, we showed that realistic magnetograms can be produced by the Pix2PixHD model, which uses both FM and GAN losses. In the present study, we use not only the FM loss but also the CC loss. The CC objective guides our model to generate the fields balancing positive and negative polarities. As a result of multiple tests with different values of importance, we set the importance of CC loss (λ_3) to be five, for which our model shows the best performance in terms of metrics and visual aspects. The importance of GAN loss in our final objectives is lower than that of Pix2PixHD. As the training of our model continues, the model gets a greater number of updates from the FM and CC loss than from the GAN loss. To minimize the objective functions, we use an adaptive moment estimation (Adam; Kingma & Ba 2014) optimizer with a learning rate 0.0002. We train the model for 1,000,000 iterations, and save the model and AI-generated data from the evaluation inputs at every 10,000th iteration. We evaluate all of the saved models by the metrics and use the highest scoring model to generate farside magnetograms. Our codes of Pix2PixCC are available at https://github.com/JeongHyunJin/Pix2PixCC, and more details of our model are described in the readme file. The codes are archived on Zenodo (Jeong 2022).

3. Data Sets

3.1. Training Data Sets

Here we use SDO/AIA EUV 304, 193, and 171 Å images and SDO/HMI LOS magnetograms to train our deep-learning model. The three EUV passbands correspond to the chromosphere, corona, and upper transition region of the Sun, respectively. We use multichannel inputs to generate target magnetograms. Channel dimensions of the inputs are composed of three EUV passband images and a reference data pair. The reference data pair is composed of three SDO/AIA images and an SDO/HMI magnetogram, which were observed one solar rotation (27.3 days) prior. We expect that the differences between the EUV images and the reference data pair give the model information on how the intensities or distributions of the magnetic fields have changed.

We use pairs of train data sets with 6 hr cadence (at 01:00, 07:00, 13:00, and 19:00 UT each day) from 2011 January 1 to 2021 June 30. We select 10 months of data per year, excluding the data sets for the evaluation of our model. The months are shifted by 4 months. Among the 2011 data sets, for example, we use data from March to December for the model training, and the remaining data from January to February for the model evaluation. We use data from 2012 January to April and from July to December to train the model, and the remaining data from May to June to evaluate the model. These data set configurations are given to consider various solar inclination conditions. The inclination of the solar rotation axis with respect to the ecliptic plane makes different distributions of southern/northern magnetic fields for each month (Pastor Yabar et al. 2015). We take 6437 pairs for the training data sets. We remove data with poor quality that are flagged by a nonzero

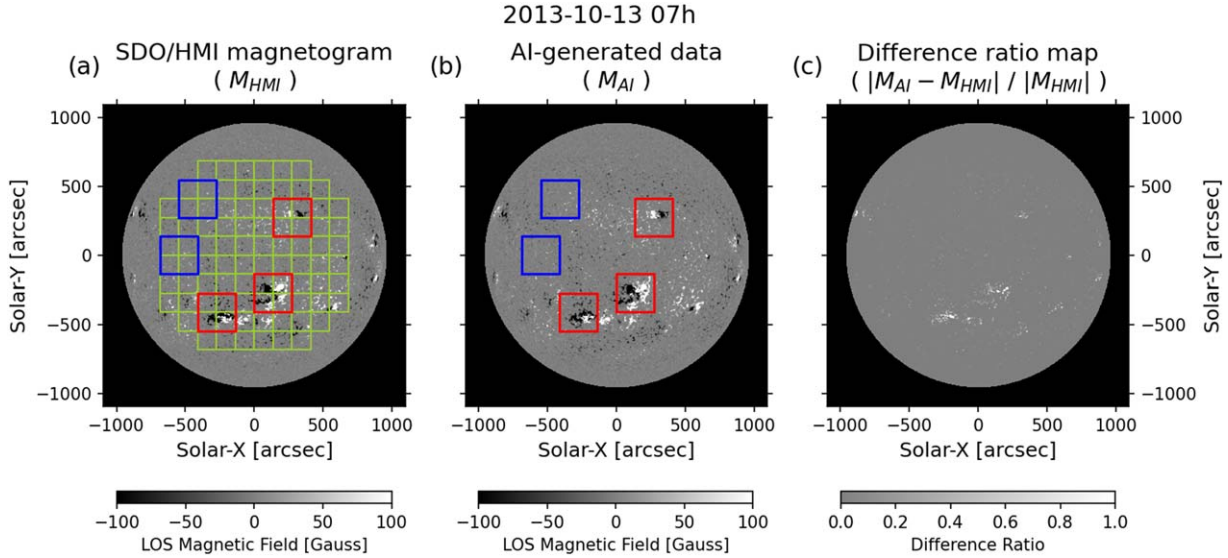

Figure 2. Automatically selected areas of AR (red boxes) and QR (blue boxes) in the SDO/HMI magnetogram acquired at 2013 October 13 07:00 UT. Polarities of the magnetic fields are displayed in white for positive and black for negative. The detected areas, each having 128×128 pixels ($\sim 273'' \times 273''$), are overlaid on AI-generated data corresponding to the real one. The green grid lines represent 64 pixel ($\sim 136\farcs5$) intervals within 60° from the center of the solar disk. An animation of this figure is available and shows the results from 2013 October 1 to November 30. In the animation, the grid lines are erased for visual comparison of the results. The real-time duration of the animation is 77 s.

(An animation of this figure is available.)

value of the QUALITY keyword for both AIA and HMI data sets. Then we align them to have the same rotational axis, pixel size of solar radius ($R_\odot$), and location of the disk center. We downsample them from 4096×4096 to 1024×1024 for computational capability. The radius of the Sun is fixed at 450 pixels. A mask is applied to the area outside 0.998 $R_\odot$ from the disk center for minimizing the uncertainty of limb data. All EUV data numbers are scaled by median values on the solar disk to calibrate the gradual in-orbit degradation of the AIA instrument (Ugarte-Urra et al. 2015; Liewer et al. 2017).

3.2. Evaluation Data Sets

We use the remaining SDO data pairs, which are 2 months of data per year, to evaluate our model. Among them, we use the pairs of data sets from 2011 to 2017 to compare with the results of KPL19 and J20. We take 1342 pairs for the evaluation data sets. The preprocessing steps of the evaluation data are the same as those of training data.

When we compute objective measures between the target magnetograms and AI-generated data to evaluate our model, we compare the results not only of data for the full disk, but also data for the ARs and QRs. We select areas of the ARs and QRs with a size of 128×128 pixels from the preprocessed target magnetograms with 1024×1024 pixel resolution. We do not consider the areas outside 60° from the disk center to exclude limb data with uncertainty. We compute the total unsigned magnetic flux (TUMF) for the area, moving at intervals of 64 pixels up, down, left, and right from the center of the solar disk. When the TUMF of the area is greater than 5×10^{21} Mx, the area is classified as an AR (Waldmeier 1955; van Driel-Gesztelyi & Green 2015). Otherwise, the areas are candidates for QRs. The boundaries of all detected areas do not overlap with one another. In order to balance the number of AR and QR areas, we select up to three AR areas for each magnetogram in the order of the largest TUMF, and up to two QR areas for each magnetogram in the order of the lowest TUMF.

Figure 2 shows an example of the selection result on 2013 October 13. There are three solar ARs near the center of the solar disk. The green grid lines in Figure 2(a) represent the boundaries of the areas where the TUMF is calculated. Our method successfully detects the approximate positions of three AR areas (red boxes in Figure 2(a)), and two QR areas (blue boxes in Figure 2(a)). Each box is placed in the same position on the AI-generated data as shown in Figure 2(b). Figure 2(c) shows a difference ratio map between the SDO/HMI magnetogram and AI-generated data. To compare the differences of their significant magnetic features, we smooth them out using a method similar to Higgins et al. (2011), who used ±70 G as a minimum threshold and a 2D Gaussian smoothing for the magnetograms; here we take 1σ and a window size of 10×10 pixels.

3.3. STEREO Data Sets

We use solar farside STEREO/EUVI EUV observations and pairs of SDO/AIA EUV images and SDO/HMI magnetograms to generate the farside magnetograms. The EUV passbands of STEREO are 304, 195, and 171 Å, which have similar temperature responses to the passbands of the SDO. We use STEREO data sets with 6 hr cadence (at 00:00, 06:00, 12:00, and 18:00 UT each day) from 2011 January 1 to 2021 June 30. Since communications with STEREO B were lost on 2014 October 1, the data from STEREO B are available until that day. We align, downsample, mask, and scale the STEREO EUV images like the SDO EUV ones. We manually exclude a set of STEREO data with incorrect header information and noise or missing values because of solar flares. The SDO pairs are data from the frontside that are selected by considering the separation angle between STEREO A (or B) and SDO. The observation dates of the reference SDO pairs are obtained by

$$T_{\mathrm{SDO}} = T_{\mathrm{STEREO}} - \Phi_{\mathrm{STEREO}} \times \frac{27.3 \text{ day}}{360^\circ}, \tag{5}$$

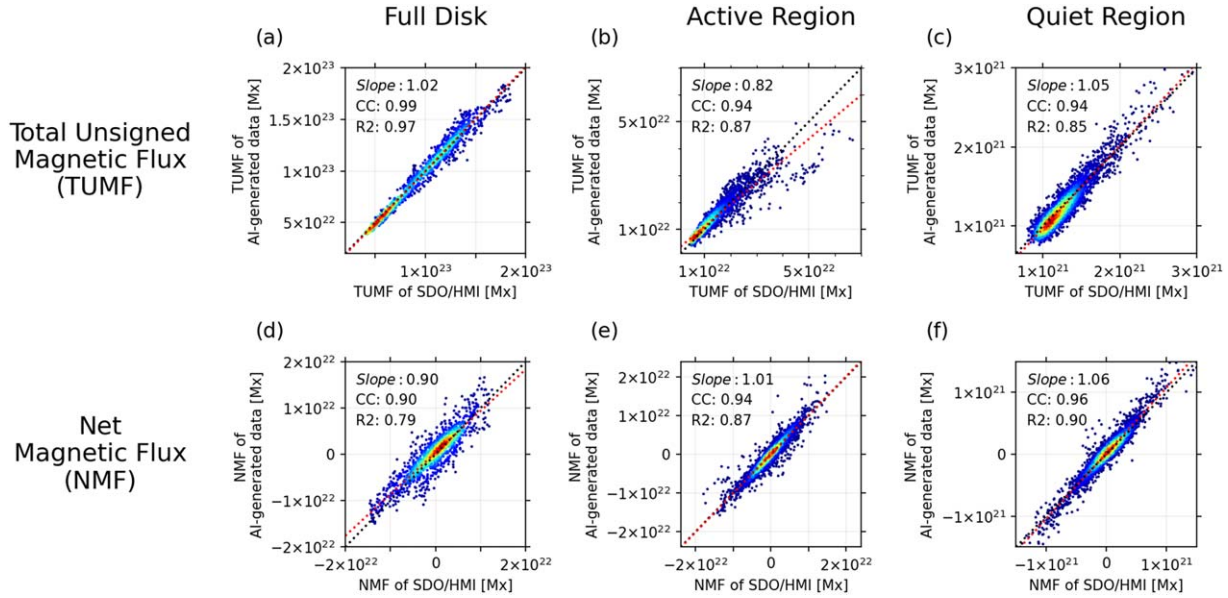

Figure 3. Two objective measures of comparisons between the SDO/HMI magnetograms and AI-generated magnetograms for 1342 full disk, 2926 ARs, and 2684 QRs. Panels (a), (b), and (c) are scatter plots between the TUMFs of the SDO/HMI magnetograms and AI-generated magnetograms for the full disk, ARs, and QRs, respectively. Panels (d), (e), and (f) are scatter plots between the NMFs of the SDO/HMI magnetograms and AI-generated magnetograms for the same data sets, respectively.

where $T_{\rm SDO}$, $T_{\rm STEREO}$, and $\Phi_{\rm STEREO}$ are the date of reference SDO pairs, the date of STEREO data sets, and heliographic longitude of the STEREO, respectively. Given these configurations, we expect that the frontside magnetograms give our model information about the overall magnetic field distribution. And the EUV image sets of the frontside SDO and the farside STEREO are used to give information about the changes of features on the Sun.

4. Results and Discussions

4.1. Evaluation of Our Deep-learning Model

We evaluate our deep-learning model using the frontside evaluation data sets that we did not use when training the model. To compare our results with KPL19 and J20, we use Pearson's CC as a measure for the evaluation. Table 1 shows the average pixel-to-pixel CCs between the SDO/HMI magnetograms and AI-generated ones with a full dynamic range. Our model shows that the average pixel-to-pixel CCs after 8×8 binning are 0.88, 0.91, and 0.70 for the 1342 full disk, 2926 ARs, and 2684 QRs, respectively. These imply that our model improves the generation of magnetograms when compared with the results of KPL19 and J20. In addition, the pixel-to-pixel CCs between the target and our AI-generated data after 4×4 binning show better results than the CCs between the target and those of KPL19 after 8×8 binning. The latitudinal or longitudinal heliographic resolution at the center of the solar disk is approximately 1° per pixel after 8×8 binning.

Figure 3 shows scatter plots between two objective measures of SDO/HMI magnetograms and AI-generated ones for the same data sets when calculating the average pixel-to-pixel CCs. We compare the TUMF between the target and AI-generated data (Figures 3(a)–(c)). The TUMF CCs are 0.99, 0.94, and 0.94, the R2 scores are 0.97, 0.87, and 0.85, and the slopes are 1.02, 0.82, and 1.05 for the full disk, ARs, and QRs, respectively. We compare net magnetic flux (NMF) between the real and AI-generated data (Figures 3(d)–(f)). The NMF CCs are 0.90, 0.94, and 0.96, the R2 scores are 0.79, 0.87, and 0.90, and the slopes are 0.90, 0.94, and 0.96 for the full disk, ARs, and QRs, respectively. Most values of TUMF and NMF fall on the diagonal line (the black dotted line in Figure 3) through the origin. These values support that our model can generate consistent magnetic fluxes.

Table 1
Average Pixel-to-pixel CCs between SDO/HMI Magnetograms and AI-generated Magnetograms for Full Disk, ARs, and QRs

	Pixel-to-pixel CC		
	8×8 Binning		
	Full Disk (1342)	AR (2926)	QR (2684)
AISFM 3.0 (Ours)	0.88	0.91	0.70
AISFM 2.0 (J20)	0.81	0.79	0.62
AISFM 1.0 (KPL19)	0.77	0.66	0.21

Note. The results of J20 and KPL19 are shown for comparison.

Figure 3(b) shows that our model slightly underestimates the TUMF of the strong ARs more than the real ones. We examine why a small portion of the ARs show underestimated TUMFs. We find that for some ARs, the AI-generated data do not produce strong magnetic fields. In these cases, the ARs do not have high intensities at 304, 193, and 171 Å images but have high intensities at 94 Å (Fe XVIII) and 131 Å (Fe VIII, XXI) of SDO/AIA. These shorter-wavelength channels are characterized by high-temperature emissions (O'dwyer et al. 2010; Warren et al. 2011). We think that the 94 and 131 Å observations are helpful in generating strong magnetic fluxes for the ARs. However, in this study, we do not use the 94 and 131 Å images to train our model because the STEREO/EUVI only have filter bands of 171, 195, 284, and 304 Å.

For the ARs, we evaluate our model based on the similarity of the AI-generated magnetograms with the real ones. We use a

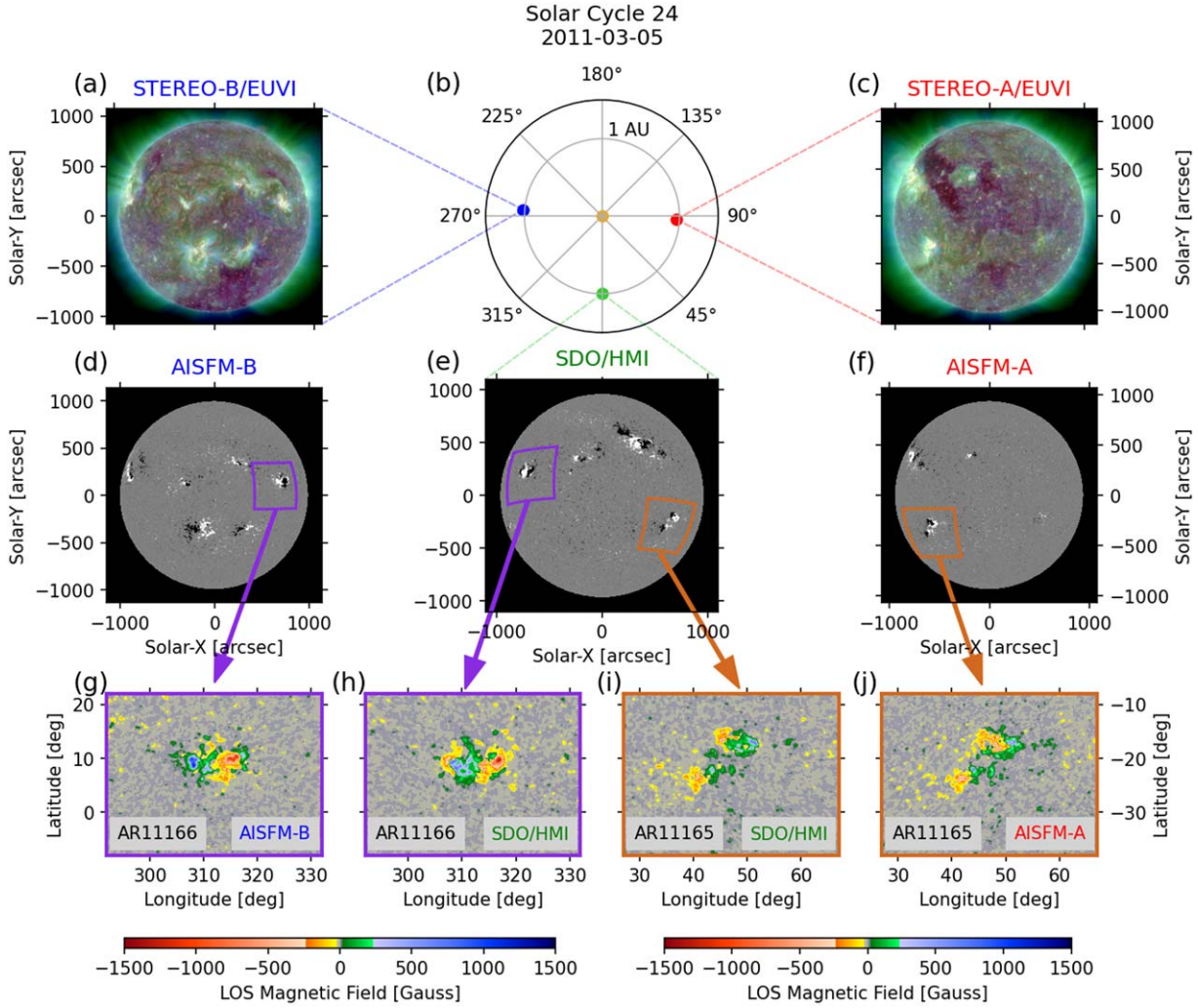

Figure 4. (a)–(f) Solar frontside SDO/HMI magnetogram, the farside STEREO composite EUV images (red: 304 Å; green: 193 Å; and blue: 171 Å), and AISFMs on 2011 March 5. The purple and brown boxes represent NOAA AR 11166 and 11165, respectively. (g)–(j) The two ARs are zoomed and converted from full disk data to heliographic coordinated maps. The color map of zoomed ARs shows the large dynamic range of values in gauss.

Structural SIMilarity (SSIM) method, which is widely used to measure the degree of similarity and consider measurements of luminance, contrast, and structure between two images. The SSIM produces a value between 0 and 1. The maximum value of 1 indicates that they show perfectly similar structure, and vice versa. We use the dynamic range of the pixel values to compute the SSIM from −1500 G to +1500 G considering our test data sets. Our model shows that the average SSIM value for the ARs is 0.74 with a standard deviation of 0.09. After 8 × 8 binning, the average SSIM value is 0.93 with a standard deviation of 0.09.

4.2. Generation of Solar Farside Magnetograms

We generate farside magnetograms from the STEREO EUV images and frontside reference data pairs from the model. The dates of AISFMs for STEREO A (AISFMs A) are from 2011 January 1 to 2021 June 30, and those of the AISFMs for STEREO B (AISFMs B) are from 2011 January 10 to 2014 September 27. In 2011 January, the position of STEREO A was about 85° longitude, and that of STEREO B was about −90° longitude in Stonyhurst heliographic coordinates. They drift away at a rate of about 22° per year from Earth.

Figure 4 shows multiviewpoint data from SDO, and STEREO A and B on 2011 March 5. The position of STEREO A is about 88° heliographic longitude near the west limb, and the position of STEREO B is about 265° heliographic longitude near the east limb of the solar frontside (Figure 4(b)). We select an NOAA AR 11165 to the west, and an NOAA AR 11166 to the east of the solar disk from the frontside SDO/HMI magnetogram (Figure 4(e)). AR 11165 is observed by STEREO A (Figure 4(c)) and AISFM A (Figure 4(f)). The TUMF of AR 11165 from the SDO/HMI magnetogram in Figure 4(i) is about 1.85×10^{22} Mx, and that from AISFM A in Figure 4(j) is about 1.74×10^{22} Mx. AR 11166 is observed by STEREO B (Figure 4(a)) and AISFM B (Figure 4(d)). The TUMF of AR11166 from the SDO/HMI magnetogram in Figure 4(h) is 2.50×10^{22} Mx, and that from AISFM B in Figure 4(g) is 2.71×10^{22} Mx. The TUMFs of the ARs from our AISFMs are consistent with those of the real one, and the distributions of the magnetic fields look like the real one.

Figure 5 shows the temporal evolution of AR 11166, which is shown in Figures 4(g)–(h). We track the AR for three solar rotations at a Carrington rotation rate. We calculate the TUMF

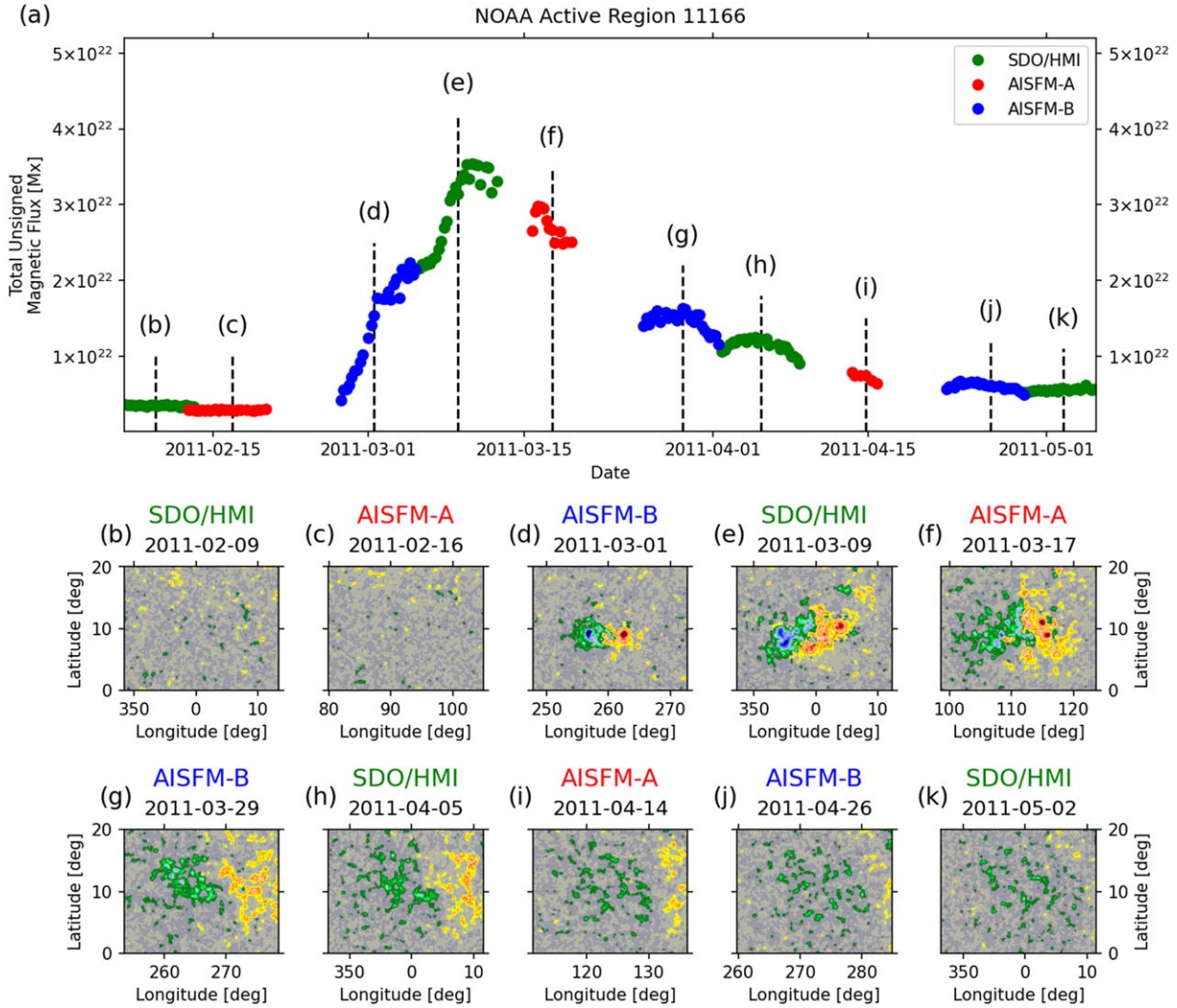

Figure 5. (a) A temporal variation of the TUMF in NOAA AR 11166 from 2011 February 1 to May 7. The green, red, and blue dots are TUMFs from SDO/HMI, AISFM A, and AISFM B, respectively. (b)–(k) A series of magnetograms tracking the AR over three solar rotations. The magnetograms are converted from full disk data to heliographic coordinated maps. The color map of the magnetic fields is the same as shown in Figures 4(g)–(j).

for each area including the AR when the HMI or AISFMs are available, and the results are shown in Figure 5(a). We consider the ARs within 60° from the disk center of the HMI or AISFMs. One impressive thing is that the TUMFs from the SDO/HMI and those from our AISFMs between solar frontside and farside are smoothly overlapped, demonstrating that it is possible to monitor the change in magnetic flux quantitatively using our method. Figures 5(b)–(k) show magnetograms of the tracked AR. Combining SDO/HMI magnetograms and AISFMs makes it possible to continuously monitor the evolution of the magnetic field distribution over the solar surface.

Figure 6 shows the tracking of ARs over the solar surface from 2012 December 7 to 2013 January 20. The ARs from SDO/HMI and AISFM A and B are converted from full disk data to heliographic coordinated maps. When the data are not available, we replace them with the nearest available ones. The position of STEREO A is about 130° heliographic longitude, and that of STEREO B is about 230° heliographic longitude. AISFM A and B show their consistent growth and decay.

Figure 7 shows comparisons between an SDO/HMI magnetogram and two AISFMs of solar cycle 25. When the solar cycle changes, all of the solar magnetic field patterns are reversed (Hale & Nicholson 1925). On 2021 May 20, the position of STEREO A is about 309° heliographic longitude (Figure 7(b)). The magnetic field polarities of our AISFM A (Figure 7(d)) are consistent with the ones of an SDO/HMI magnetogram (Figure 7(e)), which is obtained at the frontside after 4 days. As shown in Figure 7(c), AISFM 2.0 cannot produce reasonable polarities that can be identified from HMI magnetograms. It is noted that the AISFM 2.0 is generated from the STEREO A EUV observations (Figure 7(a)) without reference information from the solar frontside. The polarity distributions of AISFM 2.0 are similar to those of solar cycle 24. We mark NOAA AR 12824 with yellow dotted circles in Figures 7(c)–(e). The AR from the HMI magnetogram shows leading positive and following negative polarities. Our AISFM 3.0 represents the polarity distributions of the AR well.

Figure 8 shows comparisons between mean polar field strengths from the SDO/HMI magnetograms and those from AISFMs A and B. The results from AISFM A and B are presented at 5 day intervals. The polar fields computed from our AISFMs 3.0 follow the trend of the polar field reversal process shown by the computed results from the SDO/HMI.

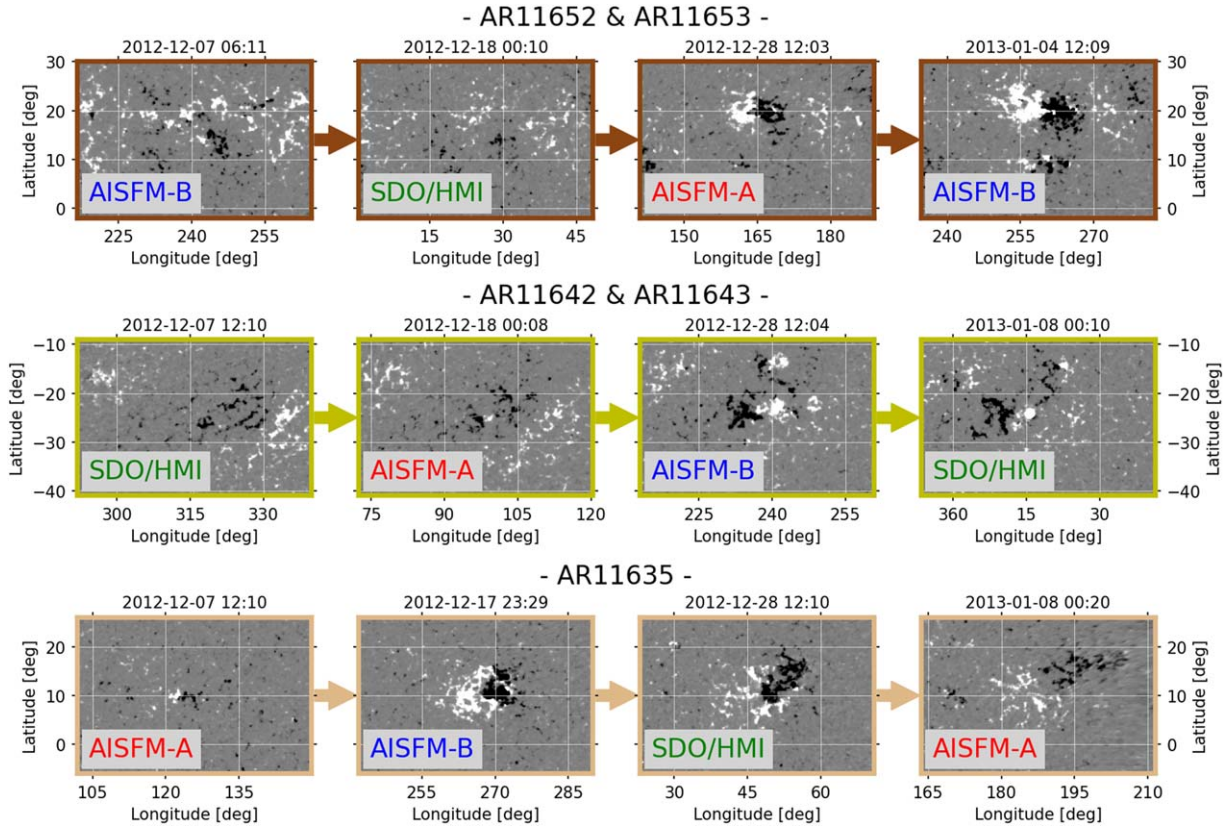

Figure 6. Temporal evolution of the ARs obtained by SDO/HMI, and AISFM A and B from 2012 December 7 to 2013 January 20. Three colored boxes denote the ARs on the solar surface. An animation of this figure is available. The real-time duration of the animation is 36 s.

(An animation of this figure is available.)

We use mean radial fields of the HMI polar field data series, hmi.meanpf_720s, which are provided from the JSOC. The LOS magnetic fields are converted to radial fields, under the assumption that the actual field vector is radial. The mean polar field strength is calculated from the values within ±45° longitude and above 60° latitude (see Sun et al. 2015 for details). We calculate mean polar fields of the AISFMs according to their study, and our results are consistent with their results.

One may ask the question, "How could one technique find the magnetic polarity distribution from EUV images?" KPL19 showed that deep learning can generate solar farside magnetograms, with Hale-patterned ARs being well replicated from the EUV 304 Å images. The pixel values, i.e., intensities, of the EUV images can give our model the distribution of magnetic fields. Ugarte-Urra et al. (2015) showed that integrated 304 Å light curves can be used as a proxy for the TUMF of the AR. Based on these results, several studies tried to generate solar magnetograms from the EUV 304 Å images using deep learning (Alshehhi 2020; Dani et al. 2022). J20 generated more realistic magnetograms using the EUV 304, 193, and 171 Å images. The EUV 193 and 171 Å passbands, which correspond to the corona and upper transition region, respectively, are widely used for detection of coronal holes (Garton et al. 2018; Linker et al. 2021). The distribution of coronal holes is related to that of open flux regions, i.e., unipolar regions (Lowder et al. 2014). The multichannel EUV images can give the model information about the distribution of not only the ARs, but also the unipolar regions related to the coronal holes. Here we use reference solar frontside magnetograms and EUV images to generate the farside magnetograms. Hale et al. (1919) noted that most leading spots have opposite polarities in opposite hemispheres. Hale's law correctly predicts polarities of the ARs about 90% of the time (Li 2018). The reference data sets give our model overall magnetic field polarity distributions including the polarities of leading spots. Based on these arguments, our model successfully generates the farside magnetograms of solar cycles 24 and 25. However, it may not be exact when the magnetic fields of the ARs do not follow Hale's law. It is especially difficult to predict the polarity distributions of rapidly emerging ARs, which were not observed at the reference data sets. Our model generates magnetograms based on a large amount of iterative training to produce accurate magnetic field distributions from the input data sets. If additional training data sets with different distributions of magnetic field polarities, various shapes of ARs, and appearances and disappearances of ARs are provided, we expect our model to be able to predict more realistic magnetograms.

5. Data Release

Here we first release the AISFMs at the KDC for SDO.[5] The names of AISFMs 3.0 A and B recorded in the AI-generated data base are aisfm_v3_stereo_a and aisfm_v3_stereo_b, respectively. There are 7913 AISFMs A from 2011 January 1 to 2021 June 30, and 2890 AISFMs B from 2011 January 10 to

[5] http://sdo.kasi.re.kr

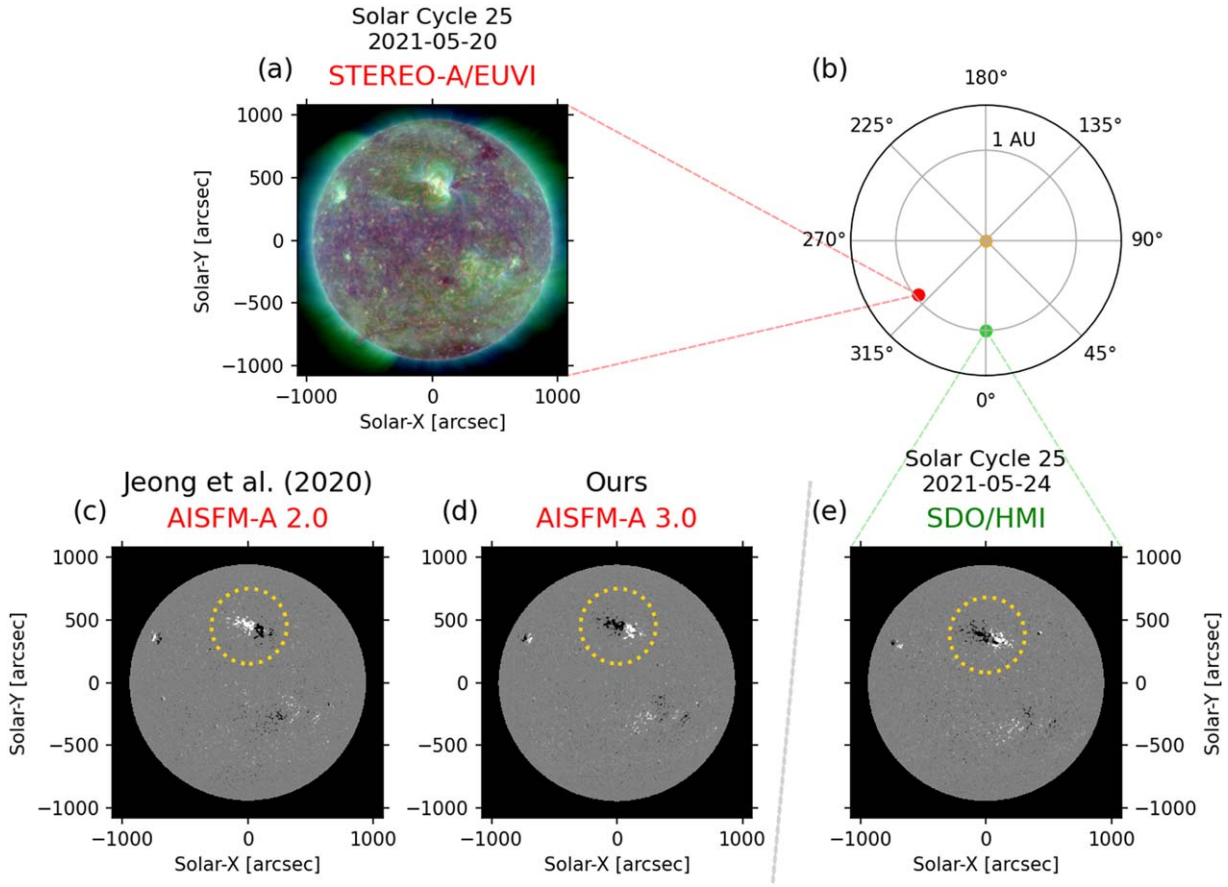

Figure 7. A solar farside STEREO A EUV image and AISFMs on 2021 May 20, and the frontside SDO/HMI magnetogram on 2021 May 24. The yellow dotted circles represent NOAA AR 12824. A result of J20 (AISFM A 2.0) is shown together for comparison with our result (AISFM A 3.0).

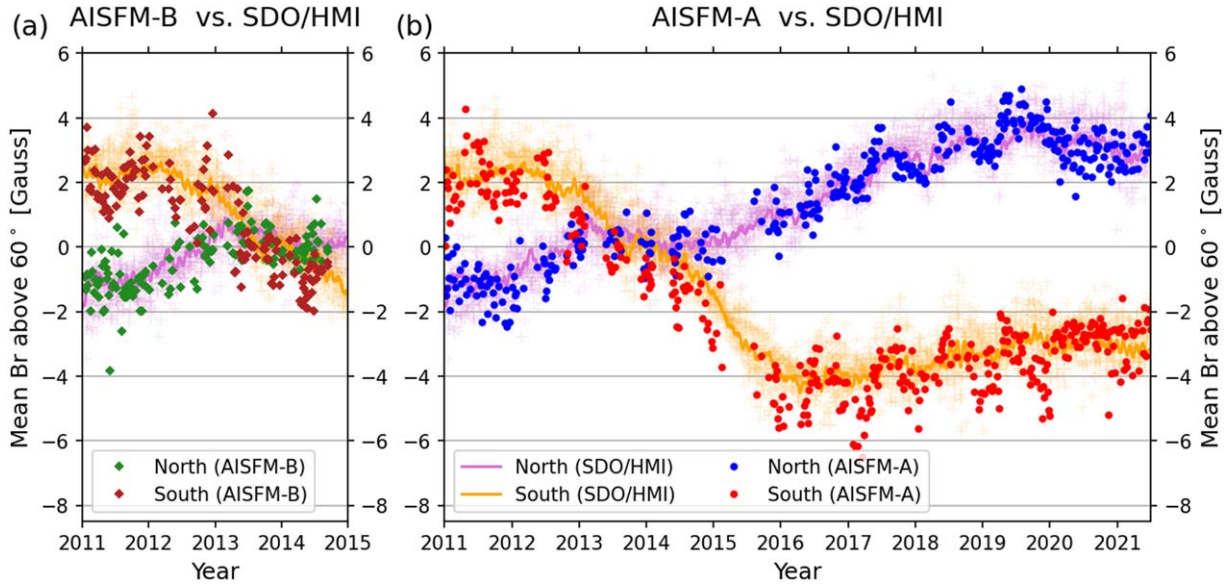

Figure 8. Comparisons of solar polar field strengths from SDO/HMI and those from AISFM A and B. Yellow (purple) dots represent the mean radial field strength above 60° in the south (north) of SDO/HMI magnetograms; the lines represent the smoothed average. Brown (green) and red (blue) dots represent the mean radial field strength above 60° in the south (north) of AISFMs A and B, respectively.

2014 September 27 with 6 hr cadence. When the model inputs from the STEREO and the SDO have poor quality data, we do not produce AISFMs. The number of AISFMs A for 2015 is smaller than that for other years, because the contact with STEREO A was interrupted as it passed behind the Sun.

The AISFMs 3.0 are saved in the flexible image transport system (FITS) format (Pence et al. 2010). The data have 1024×1024 pixels, and the solar radius is fixed at 450 pixels. The data outside the solar radius are filled with not-a-number values like those of the SDO/HMI magnetograms. The data

Table A1
Ephemeris Keywords for the AISFMs

Keyword	Description	Format or Unit
INPUTDAT	Observer of the model input data	STEREO_A (or _B)
DATE-OBS	Mean date and time of STEREO observations	universal Time
CTYPE1, CTYPE2	Helioprojective (Cartesian) system	arcseconds
HGLN_OBS, HGLT_OBS	Stonyhurst heliographic longitude and latitude of STEREO	degrees
CRLN_OBS, CRLT_OBS	Carrington heliographic longitude and latitude of STEREO	degrees
RSUN_OBS, RSUN	Observed radius of the Sun in arcseconds	arcseconds
RSUN_REF	Reference radius of the Sun	meters
R_SUN	Pixel size of the solar radius	pixels
DSUN_OBS	Distance between the center of the Sun and STEREO	meters
DSUN_REF	Average distance from the Sun to Earth (1 au)	meters

inside the solar radius represent magnetic fields along the LOS to STEREO A or B. The coordinate information of STEREO is stored in the FITS header keywords (see more details in the Appendix). We also provide example codes to understand the AISFMs at https://github.com/JeongHyunJin/AISFM3.0, and the codes are archived on Zenodo (Jeong 2022).

6. Summary and Conclusion

In this study we have generated improved solar farside magnetograms by the STEREO and SDO data sets using a deep-learning model. For this work, we have improved our model including the CC-based objectives and used model inputs on the farside STEREO EUV observations together with the frontside SDO data pairs. We selected 6437 pairs of input and target data sets from 2011 January 1 to 2021 June 30 for the model training. Targets for the training are SDO/HMI magnetograms. Inputs for the training consist of the EUV images, and the pairs of EUV images and magnetograms obtained 27.3 days prior. We have evaluated the model using test data sets not used for training.

The main results of this study are as follows. First, we improved the AI-generated magnetograms. The average pixel-to-pixel CCs between the SDO/HMI magnetograms and our AI-generated ones after 8×8 binning are 0.88, 0.91, and 0.70 for the full disk, ARs, and QRs, respectively, which are noticeably better than the previous results. We obtained good agreement between the TUMFs calculated from the SDO/HMI magnetograms and those calculated from the AI-generated ones, as well as the NMFs calculated from the HMI data and those calculated from the AI-generated ones. Second, we generate more realistic solar farside magnetograms using the STEREO EUV images and the frontside data pairs by the model. We compare the magnetic fields of ARs from the AISFMs and HMI when the positions of STEREO A and B are near the west and east limb of the solar frontside, respectively. Together with the AISFMs and HMI, we can continuously monitor the temporal evolution of the TUMF of an AR over three solar rotations. Third, our model can generate AISFMs of solar cycles 24 and 25, in which data have consistent magnetic field polarities with those of nearby frontside ones. We show that the temporal variation of the mean polar fields calculated from the AISFMs well represents the Sun's magnetic field reversal process.

Our method has several advantages over the conventional methods. First, our AISFMs can improve studies using solar magnetic flux distributions. We can track the ARs and study their flux evolution at the solar surface using the AISFMs together with the frontside magnetograms, as shown in Figure 5 (also see KPL19). Second, we can improve global coronal magnetic field extrapolation from the synchronic maps with our AISFMs. In J20, we showed that global extrapolations from the synchronic maps with AISFMs were more consistent with EUV observations than those from conventional data in view of the ARs and coronal holes. Third, we expect that our AISFMs provide better input data for heliospheric solar wind propagation models such as WSA-ENLIL (Arge & Pizzo 2000) and EUHFORIA (Pomoell & Poedts 2018). We also acknowledge that our method has a couple of limitations. First, physical quantities based on the pixel-to-pixel distribution of magnetic fields (e.g., neutral line) may not be exact. Second, small-scale magnetic field configurations, such as magnetic cancellation features, may not be well produced.

This study used a large amount of STEREO and SDO data. We appreciate numerous team members who have contributed to the success of the STEREO and SDO missions. We acknowledge the community efforts devoted to the development of the open-source packages that were used for this work. This work was supported by the Korea Astronomy and Space Science Institute (KASI) under the R&D program (project Nos. 2022-1-850-05 and 2022-1-850-08) supervised by the Ministry of Science and ICT, and the Basic Science Research Program through the NRF funded by the Ministry of Education (NRF-2020R1C1C1003892, NRF-2021R1I1A1A01049615).

Software: PyTorch (Paszke et al. 2019), NumPy (Harris et al. 2020), Matplotlib (Hunter 2007), SciPy (Virtanen et al. 2020), Astropy (Robitaille et al. 2013; Price-Whelan et al. 2018), SunPy (The SunPy Community et al. 2020).

Appendix
FITS Header Keywords

AISFMs are stored in FITS files, each with a keyword header containing the information on the data. The keywords follow World Coordinate System conventions for describing the physical coordinate values of the data pixels (Greisen & Calabretta 2002), and several ephemeris keywords are provided in Table A1. Since our data are generated by a deep-learning model, not an observational one, we store the keyword name not in OBSERVTRY (observatory) but in INPUTDAT (input data). The AISFMs are generated based on the features from three EUV images of STEREO A (or B). Thus, we record the mean date and time of the three EUV observations in the DATE-OBS keyword. More detailed information on the model inputs is stored in the HISTORY keyword.

ORCID iDs

Hyun-Jin Jeong https://orcid.org/0000-0003-4616-947X
Yong-Jae Moon https://orcid.org/0000-0001-6216-6944
Eunsu Park https://orcid.org/0000-0003-0969-286X
Harim Lee https://orcid.org/0000-0002-9300-8073
Ji-Hye Baek https://orcid.org/0000-0002-0230-4417

References

Alshehhi, R. 2020, in Proc. IEEE/CVF Conf. on Computer Vision and Pattern Recognition Workshops (Piscataway, NJ: IEEE), 204
Arge, C., & Pizzo, V. 2000, JGR, 105, 10465
Atmaja, B. T., & Akagi, M. 2021, JPhCS, 1896, 012004
Babcock, H. W. 1953, ApJ, 118, 387
Buduma, N., & Locascio, N. 2017, Fundamentals of Deep Learning: Designing Next-generation Machine Intelligence Algorithms (Sebastopol, CA: O'Reilly Media)
Caplan, R., Downs, C., & Linker, J. 2016, ApJ, 823, 53
Dani, T., Muhamad, J., Nurzaman, M., et al. 2022, JPhCS, 2214, 012016
Garton, T. M., Gallagher, P. T., & Murray, S. A. 2018, JSWSC, 8, A02
Goodfellow, I., Bengio, Y., & Courville, A. 2016, Deep Learning (Cambridge, MA: MIT Press)
Greisen, E. W., & Calabretta, M. R. 2002, A&A, 395, 1061
Hale, G. E., Ellerman, F., Nicholson, S. B., & Joy, A. H. 1919, ApJ, 49, 153
Hale, G. E., & Nicholson, S. B. 1925, ApJ, 62, 270
Harris, C. R., Millman, K. J., Van Der Walt, S. J., et al. 2020, Natur, 585, 357
Higgins, P. A., Gallagher, P. T., McAteer, R. J., & Bloomfield, D. S. 2011, AdSpR, 47, 2105
Howard, R. A., Moses, J., Vourlidas, A., et al. 2008, SSRv, 136, 67
Hunter, J. D. 2007, CSE, 9, 90
Isola, P., Zhu, J.-Y., Zhou, T., & Efros, A. A. 2017, in Proc. 2017 IEEE Conf. on Computer Vision and Pattern Recognition (Piscataway, NJ: IEEE), 1125
Jeong, H.-J. 2022, JeongHyunJin/Pix2PixCC: Pix2PixCC model: an improved image-to-image translation model to use scientific data sets, vSoftware, Zenodo, doi:10.5281/zenodo.6668849
Jeong, H.-J., Moon, Y.-J., Park, E., & Lee, H. 2020, ApJL, 903, L25
Judge, P., Rempel, M., Ezzeddine, R., et al. 2021, ApJ, 917, 27
Kaiser, M. L., Kucera, T., Davila, J., et al. 2008, SSRv, 136, 5
Kim, T., Park, E., Lee, H., et al. 2019, NatAs, 3, 397
Kingma, D. P., & Ba, J. 2014, arXiv:1412.6980
Lawrence, I., & Lin, K. 1989, Biometrics, 45, 255
Lemen, J. R., Akin, D. J., Boerner, P. F., et al. 2011, The Solar Dynamics Observatory (Berlin: Springer), 17
Li, J. 2018, ApJ, 867, 89
Liewer, P., Qiu, J., & Lindsey, C. 2017, SoPh, 292, 146
Lim, D., Moon, Y.-J., Park, E., & Lee, J.-Y. 2021, ApJL, 915, L31
Linker, J. A., Heinemann, S. G., Temmer, M., et al. 2021, ApJ, 918, 21
Liu, J., Wang, Y., Huang, X., et al. 2021, NatAs, 5, 108
Lowder, C., Qiu, J., Leamon, R., & Liu, Y. 2014, ApJ, 783, 142
Mao, X., Li, Q., Xie, H., et al. 2017, in Proc. 2017 IEEE Int. Conf. on Computer Vision (Piscataway, NJ: IEEE), 2794
Marnerides, D., Bashford-Rogers, T., & Debattista, K. 2021, Senso, 21, 4032
Müller, D., Cyr, O. S., Zouganelis, I., et al. 2020, A&A, 642, A1
O'dwyer, B., Del Zanna, G., Mason, H., Weber, M., & Tripathi, D. 2010, A&A, 521, A21
Park, E., Jeong, H.-J., Lee, H., Kim, T., & Moon, Y.-J. 2021, NatAs, 5, 111
Park, E., Moon, Y.-J., Lee, J.-Y., et al. 2019, ApJL, 884, L23
Pastor Yabar, A., Martínez González, M., & Collados, M. 2015, MNRAS, 453, L69
Paszke, A., Gross, S., Massa, F., et al. 2019, Advances in Neural Information Processing Systems 32, ed. H. Wallach et al., https://papers.nips.cc/paper/2019/hash/bdbca288fee7f92f2bfa9f7012727740-Abstract.html
Pence, W. D., Chiappetti, L., Page, C. G., Shaw, R. A., & Stobie, E. 2010, A&A, 524, A42
Pietarila, A., Bertello, L., Harvey, J., & Pevtsov, A. 2013, SoPh, 282, 91
Pomoell, J., & Poedts, S. 2018, JSWSC, 8, A35
Price-Whelan, A. M., Sipőcz, B., Günther, H., et al. 2018, AJ, 156, 123
Rana, A., Singh, P., Valenzise, G., et al. 2019, ITIP, 29, 1285
Robitaille, T. P., Tollerud, E. J., Greenfield, P., et al. 2013, A&A, 558, A33
Scherrer, P. H., Schou, J., Bush, R., et al. 2012, SoPh, 275, 207
Shin, G., Moon, Y.-J., Park, E., et al. 2020, ApJL, 895, L16
Solanki, S. K., del Toro Iniesta, J., Woch, J., et al. 2020, A&A, 642, A11
Son, J., Cha, J., Moon, Y.-J., et al. 2021, ApJ, 920, 101
Sterling, A. C., Moore, R. L., & Hara, H. 2012, ApJ, 761, 69
Sun, X., Hoeksema, J. T., Liu, Y., & Zhao, J. 2015, ApJ, 798, 114
The SunPy Community, Barnes, W. T., Bobra, M. G., et al. 2020, ApJ, 890, 68
Ugarte-Urra, I., Upton, L., Warren, H. P., & Hathaway, D. H. 2015, ApJ, 815, 90
Vallejos, R., Pérez, J., Ellison, A. M., & Richardson, A. D. 2020, Spat. Stat., 40, 100405
van Driel-Gesztelyi, L., & Green, L. M. 2015, LRSP, 12, 1
Virtanen, P., Gommers, R., Oliphant, T. E., et al. 2020, NatMe, 17, 261
Waldmeier, M. 1955, Ergebnisse und Probleme der Sonnenforschung (Leipzig: Geest & Portig)
Wang, T.-C., Liu, M.-Y., Zhu, J.-Y., et al. 2018, in Proc. 2018 IEEE Conf. on Computer Vision and Pattern Recognition (Piscataway, NJ: IEEE), 8798
Warren, H. P., Brooks, D. H., & Winebarger, A. R. 2011, ApJ, 734, 90
Wiegelmann, T., Thalmann, J. K., & Solanki, S. K. 2014, A&ARv, 22, 78
Zhou, C., Xia, C., & Shen, Y. 2021, A&A, 647, A112